

Confinement in the Transverse Field Ising Model on the Heavy Hex Lattice

Joseph Tindall¹ and Dries Sels^{1,2}

¹Center for Computational Quantum Physics, *Flatiron Institute*, New York, New York 10010, USA

²Center for Quantum Phenomena, Department of Physics, *New York University*,
726 Broadway, New York, New York 10003, USA



(Received 12 February 2024; accepted 10 September 2024; published 29 October 2024)

Inspired by a recent quantum computing experiment [Y. Kim *et al.*, *Nature (London)*, **618**, 500–5 (2023)], we study the emergence of confinement in the transverse field Ising model on a decorated hexagonal lattice. Using an infinite tensor network state optimized with belief propagation we show how a quench from a broken symmetry state leads to striking nonthermal behavior underpinned by persistent oscillations and saturation of the entanglement entropy. We explain this phenomenon by constructing a minimal model based on the confinement of elementary excitations. Our model is in excellent agreement with our numerical results. For quenches to larger values of the transverse field and/or from nonsymmetry broken states, our numerical results display the expected signatures of thermalization: a linear growth of entanglement entropy in time, propagation of correlations, and the saturation of observables to their thermal averages. These results provide a physical explanation for the unexpected classical simulability of the quantum dynamics.

DOI: [10.1103/PhysRevLett.133.180402](https://doi.org/10.1103/PhysRevLett.133.180402)

Introduction—The mechanism by which an isolated many-body quantum system is able to relax and reach “equilibrium” is now relatively well understood [1–8]. Following the eigenstate thermalization hypothesis (ETH), the relaxation of a local observable occurs because diagonal matrix elements in the energy eigenbasis are approximately constant over some energy shell of the Hilbert space, whereas off-diagonal matrix elements are random. In certain setups, however, the ETH can be violated [9–16], allowing stable, correlated phases of matter with nontrivial properties to emerge from the system’s dynamics [17–20].

Recently, a quantum computing experiment [21] simulated the discrete-time dynamics of the transverse field Ising (TFI) model on a decorated hexagonal lattice, and even for moderately large circuit depths the system was observed to retain memory of its polarized initial state. While the experiment was claimed as a case for the utility of quantum computers, a flurry of follow-up works showed that the system could actually be simulated with classical computing resources [22–28]. Despite this, an understanding of the athermal behavior observed in the experiment and a physical explanation for its unexpected simulability have not been provided.

The TFI model in one dimension with a small longitudinal field h_{\parallel} is known to be one of the simplest many-body models where athermal behavior occurs [29–35]. For $h_{\parallel} = 0$

the model is free-fermionic and, for small transverse field strength h_{\perp} , the low lying excitations above the ground state are domain walls. The longitudinal field then acts as a confining potential on these quasiparticles, resulting in bound states of pairs of domain walls. Under a quench, these states are created and remain confined on extremely long timescales. At small h_{\parallel} their decay is nonperturbative in h_{\parallel} . This phenomenon, frequently referred to as “confinement,” manifests itself through stable, persistent oscillations in the magnetization and the entanglement entropy. Such behavior has also been proposed in weakly coupled one-dimensional TFI chains [36,37]: with the weak coupling acting like a longitudinal field for a polarized initial state, in analogy to the pure one-dimensional case.

Here we consider the continuum limit of the experiment performed in Ref. [21]—the TFI Ising model on a decorated hexagonal lattice—observing confinement in a fully two-dimensional system under a quench from a symmetry broken state. We derive a minimal model involving multiple flavors of quasiparticle which agrees strongly with our state-of-the-art numerical calculations. In this setup, the ZZ coupling between spins is isotropic and the lattice has two sublattices of different coordination numbers. This makes the confinement behavior distinct from the aforementioned one-dimensional and quasi-one-dimensional [29–37] cases, being underpinned by multiple species of quasiparticles of varying size and content. The lattice structure acts as the confining potential on these excitations: increasing their size causes the confining boundary of domain walls to grow. Our results provide an explanation for the athermal behavior observed in the experiment in Ref. [21], with its unexpected classical

Published by the American Physical Society under the terms of the [Creative Commons Attribution 4.0 International](https://creativecommons.org/licenses/by/4.0/) license. Further distribution of this work must maintain attribution to the author(s) and the published article’s title, journal citation, and DOI.

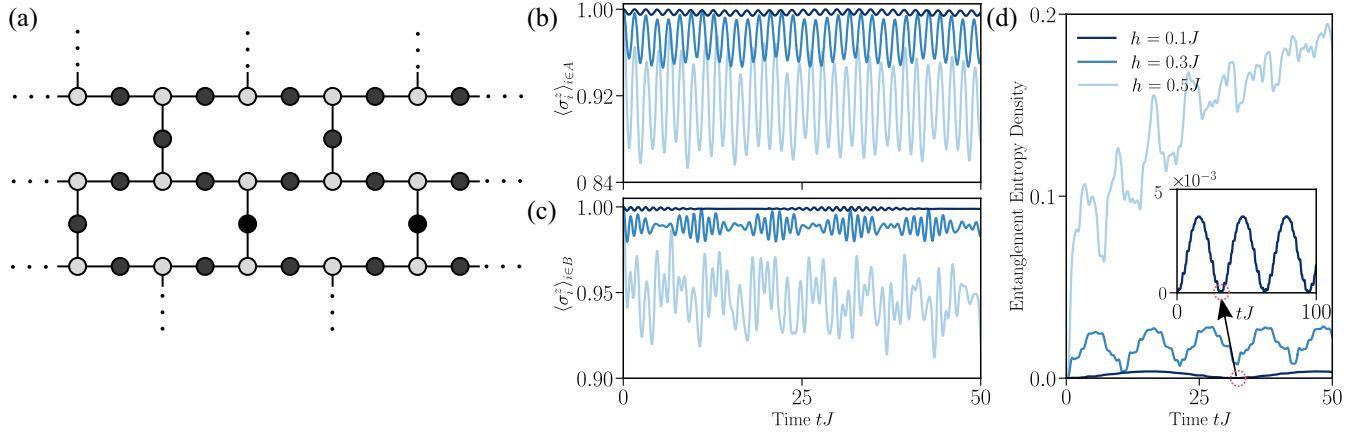


FIG. 1. (a) Finite region of the heavy hexagon lattice. The lattice is bipartite and consists of two sublattices A (dark circles) and B (light circles) which host sites of coordination number two and three, respectively. (b)–(d) Dynamics for a quench from the initial state $|Z^+\rangle = |\uparrow\uparrow\ldots\uparrow\rangle$ for $h/J = 0.1, 0.3, 0.5$ (darkest to lightest curves). (b) Dynamics of the magnetization on the A sublattice. (c) Dynamics of the magnetization on the B sublattice. (d) Dynamics of s , the density of the entanglement entropy (see Appendix for derivation). The entanglement entropy $S(A)$ between a given region A and the remainder of the lattice follows $S(A) \propto s|\partial A|$ where $|\partial A|$ is the size of the boundary between the partitions. The inset shows the dynamics of s for $h/J = 0.1$ up to $tJ \leq 100$.

simulability stemming from the localized nature of the system in the confinement regime, causing the entanglement to avoid the typical linear growth in time.

Model and numerical results—We consider the heavy hexagonal lattice: a regular hexagonal lattice where each edge is decorated with an additional lattice site. All of our results are in the limit of an infinite number of lattice sites. A view of a finite region of the heavy hex lattice is shown in Fig. (1). The lattice is bipartite with two sublattices A and B which contain sites of coordination number two and three, respectively. We are interested in the transverse field Ising Hamiltonian (setting $\hbar = 1$ throughout)

$$H = -J \sum_{\langle ij \rangle} \sigma_i^z \sigma_j^z + h \sum_i \sigma_i^x, \quad (1)$$

with σ_i^α the relevant Pauli matrix acting on lattice site i . The first summation in Eq. (1) runs over the pairs of nearest neighbors on the lattice and the second summation over all sites of the lattice.

We focus on a quench under H from the “symmetry-broken” initial state $|Z^+\rangle = |\uparrow\uparrow\ldots\uparrow\rangle$, one of the two degenerate ground states for $h = 0$. Our numerical method is to use an infinite tensor network state optimized with belief propagation (BP-iTNS). We Trotterize the exponential $U(t) = [U(\delta t)]^n = [\exp(-iH\delta t)]^n$ with $t = n\delta t$, taking δt sufficiently small to make the Trotter error negligible. The resulting sequence of gates is applied to the iTNS, performing truncations and taking expectation values using belief propagation [22,38–41]—which operates under the assumption of treelike correlations (rank-one environments) in the tensor network (see Appendix for full details of our numerical method).

The discrete-time limit of the Trotterized propagator $U(\delta t)$ with $\delta t = (\pi/4)$ and $J = 1$ on the same lattice was

directly simulated on the IBM Eagle quantum processor in Ref. [21]. The BP-iTNS method has already been shown to be extremely accurate [22,25,27] for modeling such discrete time dynamics. Here we will utilize it to simulate the continuous-time dynamics, i.e., those generated by $\lim_{\delta t \rightarrow 0} U(t)$.

In Fig. 1 we show our results for a quench for values of h up to $h \leq 0.5J$. For $h = 0.1J$ and $h = 0.3J$ we see a striking lack of thermalization, with long-lived stable oscillations appearing in both the local magnetization and the entanglement density s (see Appendix for definition). The actual Von-Neumann entanglement entropy $S(A)$ between a given region A and the rest of the lattice obeys $S(A) \propto s|\partial A|$ where $|\partial A|$ is the size of the boundary between the partition and the rest of the lattice, i.e., the number of edges connecting the two regions. For $h = 0.1J$ we observe oscillations which return the system almost exactly back to its original product state with zero entanglement. For $h = 0.5J$ in Fig. 1, we still observe persistent oscillations in the magnetization but it is decaying slowly and there is also a clear linear growth in the entanglement entropy with time: the system is slowly thermalizing on the observation timescale.

The behavior observed in Fig. 1 shows similarities with the confinement observed in one-dimensional transverse field Ising chains [29–37,42]. There, low energy excitations in the form of mesonlike quasiparticles (bound pairs of domain walls) [43] are formed on short timescales under a quench and, due to the presence of a confining potential for them, the system remains, for long times, trapped in the subspace associated with a small, noninteracting density of these quasiparticles. The confining potential can manifest itself either explicitly in the Hamiltonian via a small longitudinal field [30] or implicitly via long-range interactions [42] or a weak vertical coupling to other one-dimensional chains [36,37].

Here, we observe such oscillations on exceptionally long-time scales in the heavy hexagonal lattice. Because of the additional structure in the lattice, there are multiple low energy excitations which are relevant to the dynamics of the system and constitute different types of bound quasiparticles. The fully two-dimensional nature of the system means these quasiparticles are confined by a one-dimensional boundary of domain walls, without requiring any additional terms in the Hamiltonian. We will demonstrate this by building up a minimal model of the dynamics for small h and show how it accounts, very accurately for the dynamics observed in Fig. 1.

Confinement model—We consider the low energy excitations on top of the initial state $|Z^+\rangle$. When $h = 0$ the lowest energy excitation consists of flipping a single spin on sublattice A at an energy cost of $4J$, creating two domain walls. We notate the basis spanned by the set of states containing these single excitations with $\mathcal{A} = \{|i_A\rangle\}$ where i_A indexes the position of the flipped spin on the A sublattice. The excitations with the second lowest energy cost $6J$ and involve flipping a single spin on the B sublattice and some subset $n(i_B) \subseteq N(i_B)$ of the set of its neighbors $N(i_B)$, creating three domain walls. We notate such states as $|i_B, n(i_B)\rangle$ and define $\mathcal{B}(l)$ as the set of all basis states where a spin i_B in the lattice and a subset $n(i_B) \subseteq N(i_B)$ of fixed size l has been flipped. We have $|\mathcal{B}(l)| = N_B \binom{3}{l}$ where N_B is the total number of sites in the B sublattice. As $|N(i_B)| = 3$ we can have $l = 0, 1, 2$, or 3 and so there are five total different sets of basis states which make up the excitations with a gap $\Delta \leq 6J$ above the $h = 0$ ground state in the system.

Let us now define $|\mathcal{S}_{|\vec{k}=0}\rangle = (1/\sqrt{|\mathcal{S}|}) \sum_{s \in \mathcal{S}} |s\rangle$ as the zero-momentum state in a given set of basis states \mathcal{S} . The projector into the zero-momentum basis consisting of the five different low energy excitations is then

$$\mathcal{P}_{|\vec{k}=0} = |\mathcal{A}_{|\vec{k}=0}\rangle \langle \mathcal{A}_{|\vec{k}=0}| + \sum_{l=0}^3 |\mathcal{B}(l)_{|\vec{k}=0}\rangle \langle \mathcal{B}(l)_{|\vec{k}=0}|. \quad (2)$$

Projecting the Hamiltonian in Eq. (1) into this “confined,” zero-momentum basis gives us (see Appendix A for derivation) the following effective Hamiltonian:

$$\mathcal{P}_{|\vec{k}=0} H \mathcal{P}_{|\vec{k}=0} = \begin{pmatrix} 4J & 0 & \sqrt{2}h & 0 & 0 \\ 0 & 6J & \sqrt{3}h & 0 & 0 \\ \sqrt{2}h & \sqrt{3}h & 6J & 0 & 2h \\ 0 & 0 & 0 & 6J & \sqrt{3}h \\ 0 & 0 & 2h & \sqrt{3}h & 6J \end{pmatrix}, \quad (3)$$

for any sized heavy hexagon lattice with periodic boundary conditions—making it valid in the thermodynamic limit. The ordered (smallest to largest) eigenvalues m_1, m_2, \dots, m_5

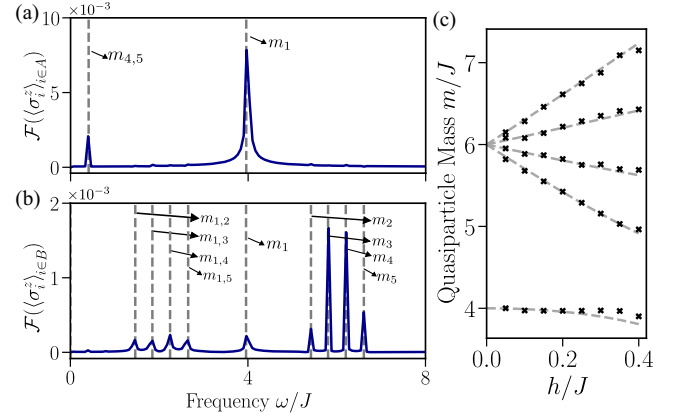


FIG. 2. (a),(b) Fourier transform for $10 \leq tJ \leq 100$ of $\langle \sigma_i^z \rangle$ on the A and B sublattices of the infinite heavy hexagon lattice. The initial state is $|Z^+\rangle = |\uparrow\uparrow\cdots\uparrow\rangle$ and is evolved under the Hamiltonian in Eq. (1) with $h = 0.2J$. Gray dotted lines indicate the quasiparticle masses m_i (and mass differences $m_{i,j} = |m_i - m_j|$) extracted from the eigenvalues of the confinement matrix in Eq. (3). (c) Masses (dashed grey lines) extracted from the confinement matrix for a range of h/J . Data points represent masses extracted from the Fourier transform of the dynamics of the magnetization calculated using iBP-TNS for $10 \leq tJ \leq 100$.

of this Hamiltonian define the masses (in units of J , as we have set $\hbar = 1$) of our quasiparticle excitations.

In Fig. 2 we plot the Fourier transform of the iBP-TNS calculated dynamics of the magnetization of the infinite system for $h = 0.2J$. We compare the frequencies present against the masses calculated from our model. We observe excellent agreement between the two, indicating our picture of confined, low energy quasiparticles is correct and further validating the iBP-TNS method for this system. In Fig. 2(c) we compare the masses against the amplitudes from the Fourier transform of the iBP-TNS dynamics for a range of values of h , observing good agreement. Discrepancies between the two become more noticeable as h increases, indicating our minimal model of confinement needs to be extended to include the ground state as well as higher order excitations which have a larger number of confining domain walls. This is consistent with the visible slow thermalization observed in Fig. 1 for $h = 0.5J$, which is a direct result of coupling to an increasing number of excitations. In the Appendix we discuss how such an extension to our model would require navigating some of the subtleties of the thermodynamic limit.

Thermalization—In Fig. 3 we compare the behavior of the system in the confinement and thermalizing regimes. To supplement our analysis and consider the spread of information in the system we calculate, under the BP approximation, the two-point correlator $C(d) = \langle \sigma_i^z \sigma_{i+d}^z \rangle - \langle \sigma_i^z \rangle \langle \sigma_{i+d}^z \rangle$ as a function of time and distance d (see Appendix for calculation details). Here we define distance d as the smallest length path (on the lattice) between two sites and, under the BP approximation, this correlator

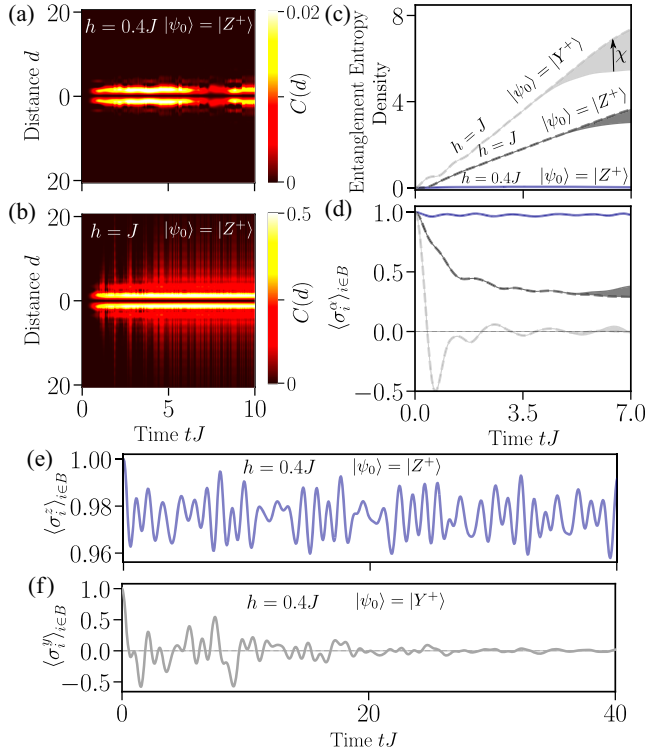


FIG. 3. (a),(b) Dynamics of the correlator $C(d) = \langle \sigma_i^z \sigma_{i+d}^z \rangle - \langle \sigma_i^z \rangle \langle \sigma_{i+d}^z \rangle$ with $i \in A$ versus d and time tJ for a quench from the initial state $|\psi_0\rangle = |Z^+\rangle$ for $h = 0.4J$ (top) and $h = J$ (bottom). The correlator is calculated under the BP approximation (see Appendix). (c),(d) Dynamics of the entanglement entropy and the on-site magnetization. The magnetization is measured along the spin axis α the initial state is polarized. Solid blue line corresponds to $|\psi_0\rangle = |Z^+\rangle$ and $h = 0.4J$, dark-gray dashed line is $|\psi_0\rangle = |Z^+\rangle$ and $h = J$ while light-gray dashed line is $|\psi_0\rangle = |Y^+\rangle$ and $h = J$. The shaded area represents results for bond dimensions $50 \leq \chi \leq 300$ of our BP-optimized iTNS (the dashed line represents the largest bond dimension used). (e),(f) Dynamics of the on-site magnetization for $h = 0.4$ and the initial states $|Y^+\rangle$ and $|Z^+\rangle$. Magnetization is measured along the spin axis the initial state is polarized along.

depends only on d and the sublattice which i belongs to. For the initial state $|Z^+\rangle$ and $h = 0.4J$ we observe a clear signature of confinement with the correlations remaining completely localized and relevant only up to very short distances. This is corroborated by persistent oscillations in the magnetization and an extremely slow growth in the entanglement entropy. For $h = J$ we instead observe the anticipated signatures of thermalization: the spreading of information (correlations) in time, a linear growth in entanglement entropy, and the saturation of $\langle \sigma_{i \in B}^z \rangle$.

We also consider the initial state $|Y^+\rangle$, where all spins are polarized along the y spin axis, which is not symmetry-broken. For $h = 0.4J$ and $h = 1.0J$ the magnetization $\langle \sigma_{i \in B}^y \rangle$ decays and settles around zero. This is consistent with the prediction from the ETH: $\langle Y^+ | H | Y^+ \rangle = 0 \forall h$ and so local observables for the initial state should relax,

under a quench, to those consistent with an infinite temperature thermal state $\rho \propto \mathbb{I}$ as it also has zero energy [$\text{Tr}(H) = 0$ due to the eigenspectrum being symmetric about 0]. We highlight the stark contrast between the dynamics of the initial states $|Z^+\rangle$ and $|Y^+\rangle$ for $h = 0.4J$ in Figs. 3(e) and 3(f), where the latter clearly relaxes while the former undergoes persistent oscillations with nondecaying amplitudes.

Truncating the iTNS—In our simulations in the confinement regime ($h \leq 0.5J$ and $|\psi_0\rangle = |Z^+\rangle$) we enforce a cutoff of $\epsilon \leq 10^{-10}$ (i.e., we discard the smallest singular values such that the sum of their squares is $\leq \epsilon$) when performing truncations on our iTNS [44]. With this we are able to keep up with the growth in bond dimension of the iTNS throughout the evolution. Outside of the confinement regime, the faster growth of entanglement entropy compared to the confinement regime means we have to actively truncate our iTNS up to a maximum bond dimension χ . We show the effect from using a range of bond dimensions in Fig. 3. As we increase the bond dimension our results converge towards the behavior predicted by the ETH.

Conclusion—We have identified the emergence of confinement in the transverse field Ising model on the heavy hexagon lattice. The more complex structure of the lattice means that, in comparison to previous work on the chain and square lattices, there are multiple types of quasiparticles which need to be accounted for to accurately identify the low energy degrees of freedom. We have presented a minimal model based on these quasiparticles—which can be straightforwardly extended to other lattices—and shown how it provides strong agreement with our state-of-the-art iBP-TNS calculations, a numerical method which also can be applied to a range of lattices [38].

Exceptionally slow thermalizing behavior was recently observed in the discrete-time dynamics generated by the same Hamiltonian on a quantum processor [21]. As discrete-time evolution breaks the conservation of energy, the rate of heating can be significantly different to that of continuous time evolution, affecting the thermalization timescale. Nonetheless, our results here indicate the physics observed on the quantum processor is that of confinement: the slow growth of entanglement, slow spreading of correlations, and memory of the initial state $|\psi_0\rangle = |\uparrow\uparrow\cdots\uparrow\rangle$ observed are all analogous to that observed in our continuous-time results here. This also explains why the BP-iTNS method [22], and a plethora of other methods [23–28] were capable of simulating the results from the quantum processor. The emergence of confinement, however, is also the reason why the physical observables measured in Ref. [21] took on nontrivial values away from their anticipated thermal predictions. Without confinement, local expectation values would have quickly been consistent with their thermal values.

We anticipate our work here can be used to analyze the role of confinement on a range of physical lattice structures. Confinement should manifest in the transverse field Ising model on any two-dimensional lattice as domains of “flipped” spins experience an energy potential proportional to the size of the boundary of the domain, which grows with domain size [45]. This potential localizes the spin excitations and the method we used here of projecting into the manifold of these low energy excitations should be valid, allowing prediction of the emergent frequencies in the confinement dynamics on a range of two-dimensional lattice structures. Arrays of Rydberg atoms, which form the building blocks of neutral atom quantum processors, represent an experimental platform where the dynamics of the TFI model can be directly realized on such a range of structures [46–49], including decorated ones where multiple flavors of quasiparticle will merge, as predicted by our theoretical work here.

Acknowledgments—J.T. and D.S. are grateful for ongoing support through the Flatiron Institute, a division of the Simons Foundation. D.S. was supported by AFOSR: Grant No. FA9550-21-1-0236. We would like to acknowledge Matt Fishman, Miles Stoudenmire, Berislav Buča, and Luka Pavesic for insightful discussions. The code used to produce the numerical results in this paper was written using the ITENSORNETWORKS.JL package [50]—a general purpose and publicly available JULIA [51] package for manipulating tensor network states of arbitrary geometry. It is built on top of ITENSORS.JL [44], which provides the basic tensor operations.

-
- [1] J. M. Deutsch, Quantum statistical mechanics in a closed system, *Phys. Rev. A* **43**, 2046 (1991).
 - [2] M. Srednicki, Chaos and quantum thermalization, *Phys. Rev. E* **50**, 888 (1994).
 - [3] M. Rigol, V. Dunjko, and M. Olshanii, Thermalization and its mechanism for generic isolated quantum systems, *Nature (London)* **452**, 854 (2008).
 - [4] H. Kim, T. N. Ikeda, and D. A. Huse, Testing whether all eigenstates obey the eigenstate thermalization hypothesis, *Phys. Rev. E* **90**, 052105 (2014).
 - [5] A. P. Luca D’Alessio, Yariv Kafri, and M. Rigol, From quantum chaos and eigenstate thermalization to statistical mechanics and thermodynamics, *Adv. Phys.* **65**, 239 (2016).
 - [6] V. Alba, Eigenstate thermalization hypothesis and integrability in quantum spin chains, *Phys. Rev. B* **91**, 155123 (2015).
 - [7] J. M. Deutsch, Eigenstate thermalization hypothesis, *Rep. Prog. Phys.* **81**, 082001 (2018).
 - [8] B. Buča, Unified theory of local quantum many-body dynamics: Eigenoperator thermalization theorems, *Phys. Rev. X* **13**, 031013 (2023).
 - [9] H. Zhao, J. Vovrosh, F. Mintert, and J. Knolle, Quantum many-body scars in optical lattices, *Phys. Rev. Lett.* **124**, 160604 (2020).
 - [10] M. Serbyn, D. A. Abanin, and Z. Papić, Quantum many-body scars and weak breaking of ergodicity, *Nat. Phys.* **17**, 675 (2021).
 - [11] C. J. Turner, A. A. Michailidis, D. A. Abanin, M. Serbyn, and Z. Papić, Weak ergodicity breaking from quantum many-body scars, *Nat. Phys.* **14**, 745 (2018).
 - [12] P. Zhang *et al.*, Many-body Hilbert space scarring on a superconducting processor, *Nat. Phys.* **19**, 120 (2023).
 - [13] B. Buča, J. Tindall, and D. Jaksch, Non-stationary coherent quantum many-body dynamics through dissipation, *Nat. Commun.* **10**, 1730 (2019).
 - [14] J. Tindall, C. S. Muñoz, B. Buča, and D. Jaksch, Quantum synchronisation enabled by dynamical symmetries and dissipation, *New J. Phys.* **22**, 013026 (2020).
 - [15] M. Medenjak, B. Buča, and D. Jaksch, Isolated Heisenberg magnet as a quantum time crystal, *Phys. Rev. B* **102**, 041117 (R) (2020).
 - [16] N. P. Konstantinidis, Thermalization away from integrability and the role of operator off-diagonal elements, *Phys. Rev. E* **91**, 052111 (2015).
 - [17] F. Iemini, A. Russomanno, J. Keeling, M. Schirò, M. Dalmonte, and R. Fazio, Boundary time crystals, *Phys. Rev. Lett.* **121**, 035301 (2018).
 - [18] J. Tindall, F. Schlawin, M. Buzzi, D. Nicoletti, J. R. Coulthard, H. Gao, A. Caviglioli, M. A. Sentef, and D. Jaksch, Dynamical order and superconductivity in a frustrated many-body system, *Phys. Rev. Lett.* **125**, 137001 (2020).
 - [19] D. V. Else, C. Monroe, C. Nayak, and N. Y. Yao, Discrete time crystals, *Annu. Rev. Condens. Matter Phys.* **11**, 467 (2020).
 - [20] Y. Bahri, R. Vosk, E. Altman, and A. Vishwanath, Localization and topology protected quantum coherence at the edge of hot matter, *Nat. Commun.* **6**, 7341 (2015).
 - [21] Y. Kim, A. Eddins, S. Anand, K. X. Wei, E. van den Berg, S. Rosenblatt, H. Nayfeh, Y. Wu, M. Zaletel, K. Temme, and A. Kandala, Evidence for the utility of quantum computing before fault tolerance, *Nature (London)* **618**, 500 (2023).
 - [22] J. Tindall, M. Fishman, E. M. Stoudenmire, and D. Sels, Efficient tensor network simulation of IBM’s eagle kicked Ising experiment, *PRX Quantum* **5**, 010308 (2024).
 - [23] S. Anand, K. Temme, A. Kandala, and M. Zaletel, Classical benchmarking of zero noise extrapolation beyond the exactly-verifiable regime, [arXiv:2306.17839](https://arxiv.org/abs/2306.17839).
 - [24] T. Begušić, J. Gray, and G. K.-L. Chan, Fast and converged classical simulations of evidence for the utility of quantum computing before fault tolerance, *Sci. Adv.* **10**, eadk4321 (2024).
 - [25] T. Begušić, J. Gray, and G. K.-L. Chan, Fast and converged classical simulations of evidence for the utility of quantum computing before fault tolerance, *Sci. Adv.* **10**, eadk4321 (2024).
 - [26] K. Kechedzhi, S. V. Isakov, S. Mandrà, B. Villalonga, X. Mi, S. Boixo, and V. Smelyanskiy, Effective quantum volume, fidelity and computational cost of noisy quantum processing experiments, *Future Gener. Comput. Syst.* **153**, 431 (2024).
 - [27] H.-J. Liao, K. Wang, Z.-S. Zhou, P. Zhang, and T. Xiang, Simulation of IBM’s kicked Ising experiment with projected entangled pair operator, [arXiv:2308.03082](https://arxiv.org/abs/2308.03082).

- [28] M. S. Rudolph, E. Fontana, Z. Holmes, and L. Cincio, Classical surrogate simulation of quantum systems with LOWESA, [arXiv:2308.09109](#).
- [29] S. Birkammer, A. Bastianello, and M. Knap, Prethermalization in one-dimensional quantum many-body systems with confinement, *Nat. Commun.* **13**, 7663 (2022).
- [30] M. Kormos, M. Collura, G. Takács, and P. Calabrese, Real-time confinement following a quantum quench to a non-integrable model, *Nat. Phys.* **13**, 246 (2017).
- [31] B. Lake, A. M. Tsvelik, S. Notbohm, D. Alan Tennant, T. G. Perring, M. Reehuis, C. Sekar, G. Krabbes, and B. Büchner, Confinement of fractional quantum number particles in a condensed-matter system, *Nat. Phys.* **6**, 50 (2010).
- [32] N. J. Robinson, A. J. A. James, and R. M. Konik, Signatures of rare states and thermalization in a theory with confinement, *Phys. Rev. B* **99**, 195108 (2019).
- [33] S. Pai and M. Pretko, Fractons from confinement in one dimension, *Phys. Rev. Res.* **2**, 013094 (2020).
- [34] S. Scopu, P. Calabrese, and A. Bastianello, Entanglement dynamics in confining spin chains, *Phys. Rev. B* **105**, 125413 (2022).
- [35] P. P. Mazza, G. Peretto, A. Lerose, M. Collura, and A. Gambassi, Suppression of transport in nondisordered quantum spin chains due to confined excitations, *Phys. Rev. B* **99**, 180302(R) (2019).
- [36] F. B. Ramos, M. Lencsés, J. C. Xavier, and R. G. Pereira, Confinement and bound states of bound states in a transverse-field two-leg Ising ladder, *Phys. Rev. B* **102**, 014426 (2020).
- [37] A. J. A. James, R. M. Konik, and N. J. Robinson, Non-thermal states arising from confinement in one and two dimensions, *Phys. Rev. Lett.* **122**, 130603 (2019).
- [38] J. Tindall and M. Fishman, Gauging tensor networks with belief propagation, *SciPost Phys.* **15**, 222 (2023).
- [39] M. Leifer and D. Poulin, Quantum graphical models and belief propagation, *Ann. Phys. (Amsterdam)* **323**, 1899 (2008).
- [40] S. Sahu and B. Swingle, Efficient tensor network simulation of quantum many-body physics on sparse graphs, [arXiv:2206.04701](#).
- [41] C. Guo, D. Poletti, and I. Arad, Block belief propagation algorithm for 2d tensor networks, *Phys. Rev. B* **108**, 125111 (2023).
- [42] F. Liu, R. Lundgren, P. Titum, G. Pagano, J. Zhang, C. Monroe, and A. V. Gorshkov, Confined quasiparticle dynamics in long-range interacting quantum spin chains, *Phys. Rev. Lett.* **122**, 150601 (2019).
- [43] T. Sulejmanpasic, H. Shao, A. W. Sandvik, and M. Ünsal, Confinement in the bulk, deconfinement on the wall: Infrared equivalence between compactified QCD and quantum magnets, *Phys. Rev. Lett.* **119**, 091601 (2017).
- [44] M. Fishman, S. R. White, and E. M. Stoudenmire, Codebase release 0.3 for ITensor, *SciPost Phys. Codebases* **4** (2022).
- [45] L. Pavešić, D. Jaschke, and S. Montangero, Constrained dynamics and confinement in the two-dimensional quantum Ising model, [arXiv:2406.11979](#).
- [46] H. Labuhn, D. Barredo, S. Ravets, S. de Léséleuc, T. Macrì, T. Lahaye, and A. Browaeys, Tunable two-dimensional arrays of single Rydberg atoms for realizing quantum Ising models, *Nature (London)* **534**, 667 (2016).
- [47] V. Lienhard, S. de Léséleuc, D. Barredo, T. Lahaye, A. Browaeys, M. Schuler, L.-P. Henry, and A. M. Läuchli, Observing the space- and time-dependent growth of correlations in dynamically tuned synthetic Ising models with antiferromagnetic interactions, *Phys. Rev. X* **8**, 021070 (2018).
- [48] A. Browaeys and T. Lahaye, Many-body physics with individually controlled Rydberg atoms, *Nat. Phys.* **16**, 132 (2020).
- [49] Y. Song, M. Kim, H. Hwang, W. Lee, and J. Ahn, Quantum simulation of Cayley-tree Ising Hamiltonians with three-dimensional Rydberg atoms, *Phys. Rev. Res.* **3**, 013286 (2021).
- [50] ITENSORNETWORKS.JL, <https://github.com/mtfishman/ITensorNetworks.jl> (2023).
- [51] J. Bezanson, A. Edelman, S. Karpinski, and V. B. Shah, JULIA: A fresh approach to numerical computing, *SIAM Rev.* **59**, 65 (2017).

End Matter

Appendix A: Deriving the confinement Hamiltonian— Here we derive the form of the effective Hamiltonian $H_{\text{eff}} = \mathcal{P}_{|\vec{k}|=0} H \mathcal{P}_{|\vec{k}|=0}$ given in Eq. (3) of the main text. This is the projection of the transverse field Ising Hamiltonian $H = -J \sum_{\langle ij \rangle} \sigma_i^z \sigma_j^z + h \sum_i \sigma_i^x = H_{ZZ} + H_X$ on any heavy hex lattice with periodic boundary conditions using the projector

$$\mathcal{P}_{|\vec{k}|=0} = |\mathcal{A}_{|\vec{k}|=0}\rangle \langle \mathcal{A}_{|\vec{k}|=0}| + \sum_{l=0}^3 |\mathcal{B}(l)_{|\vec{k}|=0}\rangle \langle \mathcal{B}(l)_{|\vec{k}|=0}|. \quad (\text{A1})$$

We have defined the normalized basis vectors

$$|\mathcal{A}_{|\vec{k}|=0}\rangle = \frac{1}{\sqrt{N_A}} \sum_{i_A \in A} |i_A\rangle, \quad |\mathcal{B}(l)_{|\vec{k}|=0}\rangle = \frac{1}{\sqrt{\binom{3}{l} N_B}} \sum_{i_B \in B} \sum_{n(i_B) \in [N(i_B)]^l} |i_B, n(i_B)\rangle \quad (\text{A2})$$

using N_A to denote the number of sites in sublattice A and N_B the number of sites in sublattice B . We use i_A and i_B to refer to spins in the A and B sublattices, respectively. The set $N(i_B)$ refers to the set of three neighbors of a spin i_B and we use the notation $[N(i_B)]^l$ to define the set of subsets of $N(i_B)$ of fixed size l . The ket $|i_B, n(i_B)\rangle$ then refers to the state where the spin i_B and the subset $n(i_B)$ are flipped with respect to the

background reference state $|Z^+\rangle = |\uparrow\uparrow\uparrow\ldots\uparrow\rangle$, which is the ground state for $h = 0$.

The state $|\mathcal{A}_{|\vec{k}|=0}\rangle$ is the first zero-momentum excited state above the ground state with excitation energy $2J \times 2 = 4J$ due to each flipped spin on the A sublattice having two neighbors with which they are then antialigned: thus creating two domain walls of energy $2J$. Meanwhile the remaining basis states are at zero momentum and have excitation energy $2J \times 3 = 6J$, due to every basis vector containing three domain walls. We therefore have

$$\mathcal{P}_{|\vec{k}|=0} H_{ZZ} \mathcal{P}_{|\vec{k}|=0} = \text{Diag}(4J, 6J, 6J, 6J, 6J) \quad (\text{A3})$$

where, without loss of generality, we have set the energy of the state $|Z^+\rangle$ to 0 and ordered the basis states as $|\mathcal{A}_{|\vec{k}|=0}\rangle, |\mathcal{B}(l=0)_{|\vec{k}|=0}\rangle, \dots, |\mathcal{B}(l=3)_{|\vec{k}|=0}\rangle$.

Now we wish to determine the projection $\mathcal{P}_{|\vec{k}|=0} H_X \mathcal{P}_{|\vec{k}|=0}$. The only nonzero terms are those for pairs of basis states which have ± 1 one more or one less flipped spin than each other. Consider, for example, the nonzero term $\langle \mathcal{B}(1)_{|\vec{k}|=0} | H_X | \mathcal{A}_{|\vec{k}|=0} \rangle$. We have

$$H_X |\mathcal{A}_{|\vec{k}|=0}\rangle = \frac{h}{\sqrt{N_A}} \sum_{i_A \in A} \sum_{i'_A \in \Lambda \setminus \{i_A\}} |i'_A, i_A\rangle, \quad (\text{A4})$$

where we use $\Lambda \setminus \{i_A\}$ to denote the set of all lattice sites excluding i_A . Now observe that independent of i_A , exactly two of the terms in $\sum_{i'_A \in \Lambda \setminus \{i_A\}} |i'_A, i_A\rangle$ will match a term in the double summation for $|\mathcal{B}(l=1)_{|\vec{k}|=0}\rangle$ [see Eq. (A2)]. We thus have

$$\langle \mathcal{B}(0)_{|\vec{k}|=0} | H_X | \mathcal{A}_{|\vec{k}|=0} \rangle = \frac{2N_A}{\sqrt{3N_A N_B}} = 2h \sqrt{\frac{N_A}{3N_B}}. \quad (\text{A5})$$

We can make similar counting arguments (although we spare the full details) to get the full list of nonzero terms (not including their conjugates)

$$\begin{aligned} \langle \mathcal{B}(l=0)_{|\vec{k}|=0} | H_X | \mathcal{A}_{|\vec{k}|=0} \rangle &= 2h \sqrt{\frac{N_A}{3N_B}}, \\ \langle \mathcal{B}(l=1)_{|\vec{k}|=0} | H_X | \mathcal{B}(l=0)_{|\vec{k}|=0} \rangle &= \sqrt{3}h, \\ \langle \mathcal{B}(l=2)_{|\vec{k}|=0} | H_X | \mathcal{B}(l=1)_{|\vec{k}|=0} \rangle &= 2h, \\ \langle \mathcal{B}(l=3)_{|\vec{k}|=0} | H_X | \mathcal{B}(l=2)_{|\vec{k}|=0} \rangle &= \sqrt{3}h. \end{aligned} \quad (\text{A6})$$

Lastly, consider the ratio $\sqrt{(N_A/N_B)}$. It is clear that for the finite unit cell [see Fig. 4(a)] we have $(N_A/N_B) = \frac{3}{2}$. This ratio will hold true for any realization of the periodic boundary heavy hex lattice, as it is simply a tiling of this unit cell with additional edges added to create the periodic boundary conditions. This gives us

$$\mathcal{P}_{|\vec{k}|=0} H_X \mathcal{P}_{|\vec{k}|=0} = \begin{pmatrix} 0 & 0 & \sqrt{2}h & 0 & 0 \\ 0 & 0 & \sqrt{3}h & 0 & 0 \\ \sqrt{2}h & \sqrt{3}h & 0 & 0 & 2h \\ 0 & 0 & 0 & 0 & \sqrt{3}h \\ 0 & 0 & 2h & \sqrt{3}h & 0 \end{pmatrix} \quad (\text{A7})$$

and finally

$$\mathcal{P}_{|\vec{k}|=0} H \mathcal{P}_{|\vec{k}|=0} = \begin{pmatrix} 4J & 0 & \sqrt{2}h & 0 & 0 \\ 0 & 6J & \sqrt{3}h & 0 & 0 \\ \sqrt{2}h & \sqrt{3}h & 6J & 0 & 2h \\ 0 & 0 & 0 & 6J & \sqrt{3}h \\ 0 & 0 & 2h & \sqrt{3}h & 6J \end{pmatrix} \quad (\text{A8})$$

in agreement with Eq. (3) of the main text—where we have ignored the constant E_0 on the diagonal as it simply shifts all the eigenvalues and is irrelevant.

Extending our projective method here to different lattices is straightforward.

We should point out that we have not included the ground state of the system in our confinement model. This is because the matrix elements coupling the ground state and the lowest excited states scale as $\mathcal{O}(\sqrt{L})$ as the thermodynamic limit $L \rightarrow \infty$ is taken with L the number of lattice sites. Thus we would need to work in a basis involving a finite “density” of spin excitations on an infinite lattice to avoid this. Our results here show that despite not including the lowest state we are able to accurately capture the emergent frequencies in the dynamics for small h , suggesting the eigenenergies we obtain are accurate and the gap to the ground state is not strongly dependent on h in this regime. By navigating some of the subtleties of the thermodynamic limit and including the ground state a more complete model may be producible which accounts for the level repulsion emerging around $h/J \sim 0.3$ in Fig. 2 of the main text and also allows us to predict the amplitude of the oscillations in the dynamics.

Appendix B: Numerical details—Our tensor network state (TNS) is the unit cell of the infinite heavy hex lattice [see Fig. 4(a)] with periodic boundary conditions [38]. The Hamiltonian in Eq. (1) is taken over this unit cell and its exponential is Trotterized to second order into a product of two-site and one-site gates with time step $\delta t J = 0.05$. The gates in $U(t)$ are applied in sequence to the initial TNS of bond-dimension one. Single-site gates are applied directly and two-site gates are applied via the simple update procedure (see Fig. 4): using belief propagation on the TNS to identify the optimal rank-one environments. The “entanglement

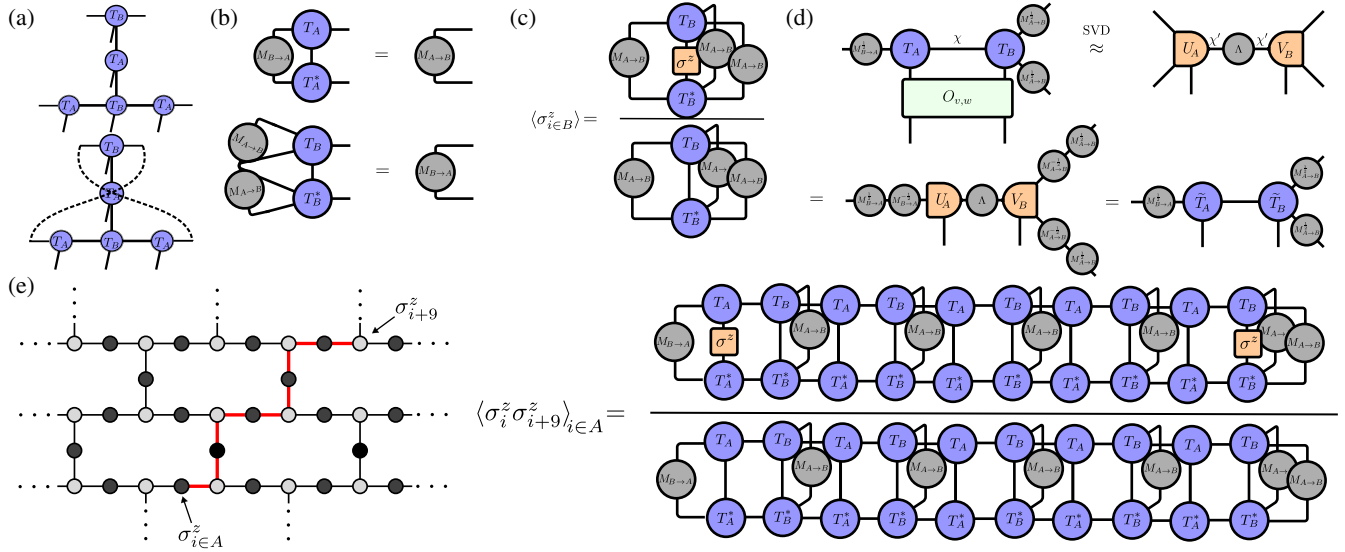


FIG. 4. (a) Top: tensor network state (TNS) over a unit cell of the infinite heavy hexagonal lattice. The lattice is characterized by two distinct tensors T_A and T_B which have two and three virtual bond indices, respectively. Bottom: TNS optimized during our simulations. The dotted lines represent edges added to create the necessary periodic boundary conditions for the simulation to map to the results of the thermodynamic limit. (b) The two unique belief propagation equations for updating the two possible message tensors. (c) Calculation of an on-site expectation value on the B sublattice using the message tensors. (d) “Simple update” procedure for applying a two-site gate on an edge of the TNS for the infinite heavy hex lattice using the square roots of the message tensors found via belief propagation. Further details can be found in Ref. [38]. (e) Method for calculating a two-point correlator $\langle \sigma_i^z \sigma_{i+d}^z \rangle$. The path between sites i and $j = i + d$ on the infinite heavy hex lattice is identified and a finite 1D TNS is constructed along that path using the tensors T_A and T_B . Message tensors are applied as environments along the bonds of the lattice broken by that path.

entropy density” is calculated as $s = -\sum_{\lambda} \lambda^2 \log_2(\lambda^2)$ where λ are the diagonal entries of the bond tensor (which are identical on each edge of the lattice) found by transforming the TNS into the Vidal gauge. This transformation can be done with the message tensors found from belief propagation [38]. Our method with this small unit cell immediately recovers the results from optimizing the TNS of the infinite heavy hex lattice with

BP, hence why we refer to it as “BP-iTNS.” Figure 4 also shows how we compute the correlation $\langle \sigma_i^z \sigma_{i+d}^z \rangle$ from the iBP-TNS, where $i + d$ indicates a site at a distance (in terms of the path length through the lattice) d from site i . We have ensured that all of our results in the main text are converged in bond dimension in comparison to the scale of the plot.